Journal of Materials Chemistry C

ROYAL SOCIETY OF CHEMISTRY

PAPER

View Article Online
View Journal

Cite this: DOI: 10.1039/d5tc03681j

Zwitterion-derived ligand-coated ZnO quantum dots engineered *via* an organometallic approach

Zygmunt Drużyński, [a] Małgorzata Wolska-Pietkiewicz *[a] and Janusz Lewiński *[ab]

Received 11th October 2025,
Accepted 20th January 2026

DOI: 10.1039/d5tc03681j

rsc.li/materials-c

Wet-organometallic approaches offer a versatile platform for the synthesis of high-quality zinc oxide quantum dots (ZnO QDs), yet remain underutilised compared with conventional sol–gel approaches. In this work, we develop an organometallic strategy based on zwitterionic ligands to expand the library of surface chemistries available for ZnO nanostructures with tailored optical and colloidal properties. By employing a classical one-pot, self-supporting organometallic method with controlled variation of the oxygen source (air or water), a series of ZnO QDs stabilised with short- and long-chain betaines is obtained. The zwitterionic ligands provide enhanced solubility and excellent colloidal stability across a broad range of solvents, enabling a systematic investigation of ligand–nanocrystal interactions. We demonstrate that both the ligand structure and the synthetic pathway, namely air exposure *versus* controlled water addition, significantly influence particle size, surface passivation, and photoluminescence quantum yield, which reaches up to 41.8%. These results establish zwitterion-derived ligands as an effective tool for engineering highly luminescent and processable ZnO QDs, offering new opportunities for next-generation ZnO-based technologies.

1. Introduction

Zinc oxide is among the most versatile and extensively studied inorganic materials, offering broad application potential and enduring relevance across multiple disciplines.[1–6] In particular, colloidal quantum-sized ZnO crystals, commonly referred to as quantum dots (QDs), exhibit unique optical properties along with functional tunability that is largely determined by their surface ligands.[6,7] Among the various wet-chemical methods for their synthesis, the sol–gel method remains one of the most widely adopted synthetic routes in contemporary research on ZnO-based nanomaterials.[8–11] This approach has been investigated for decades, starting with the seminal independent works by Hoffmann and Spanhel, who employed zinc acetate as a conventional precursor in the presence of an alkali hydroxide and an alcohol.[8,12] The size, morphology, and physicochemical properties of the sol–gel-derived ZnO nanostructures can be finely tuned by adjusting reaction parameters, such as the solvent type, salt concentration, pH, reaction time, and temperature, or by introducing external additives, including capping agents or surfactants.[4,10,11,13] However, the sol–gel method has notable limitations, such as low reproducibility caused mainly by rapid nucleation, which complicates precise control over nanocrystal growth during the initial stages. Consequently, highly irregular nanostructures with non-uniform surface coverage are often produced,[14] while residual alkali metal cations contaminate both the inorganic core and the inorganic–organic interface.[15] These challenges have stimulated interest in alternative synthetic strategies that provide greater control and purity in nanocrystal fabrication.

Among organometallic strategies for the synthesis of zinc oxide quantum dots (ZnO QDs), a notable advancement is the one-pot self-supporting organometallic (OSSOM) method, originally developed by our group. In this approach, [RZn-X]-type alkyl zinc complexes (where R denotes an alkyl or aryl group and X is a monoanionic organic ligand, *e.g.*, carboxylates,[16–21] aminoalcoholates,[22] benzamidines,[23–25] and organophosphorous[14,17,26,27] ligands) are generated *in situ* or isolated in crystalline form.[26,28,29] This method affords ZnO QDs stabilized by a densely packed and highly ordered organic shell, resulting in excellent colloidal stability and allowing for post-synthetic surface functionalization without compromising luminescent properties.[18,20,30] While sol–gel and organometallic wet-chemical techniques may utilize similar ligands, they generally fail to achieve the same degree of surface passivation or functionalization versatility.[14,18] This observation highlights that the synthetic route itself plays a crucial role in defining nanomaterial quality; however, it also underscores the

[a] *Faculty of Chemistry, Warsaw University of Technology, Noakowskiego 3, 00-664 Warsaw, Poland. E-mail: malgorzata.pietkiewicz@pw.edu.pl, janusz.lewinski@pw.edu.pl*

[b] *Institute of Physical Chemistry, Polish Academy of Sciences, Kasprzaka 44/52, 01-224 Warsaw, Poland*

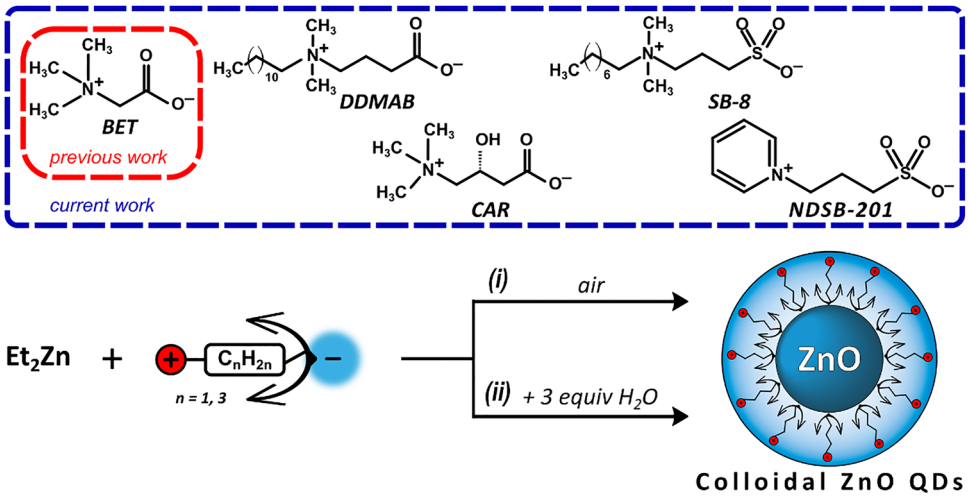

Scheme 1 Schematic representation of selected zwitterionic-type proligands and preparation of the zwitterion-derived ligand-coated ZnO QDs *via* two synthetic routes: air-exposure (path *i*) and controlled water addition method (path *ii*).

parallel challenge of selecting appropriate surface ligands, which not only stabilise the surface but also govern critical parameters such as particle size distribution, morphology, interparticle interactions, solution stability, and the accessibility of surface sites for further functionalization.[31–34]

Alternatively, homoleptic dialkylzincs (R_2Zn) constitute an efficient class of precursors for the synthesis of colloidal ZnO QDs,[35–44] analogous to the use of alkylcadmium precursors in Bawendi's hot-injection method of the synthesis of CdX quantum dots (where X = S, Se, or Te).[45] In such approaches, R_2Zn compounds are typically employed in the presence of neutral L-type ligands such as phosphines or long-chain amines.[35–38] The excess ligand often serves not only as a coordinating agent but also as a solvent and a modulator of crystal growth, enabling control over particle size, morphology, and dispersity. Despite its synthetic efficiency and the quality of the resulting nanocrystals, this method remains relatively underutilized in comparison to more conventional sol–gel techniques. More recently, our group has proposed an alternative strategy for the ambient-temperature synthesis of colloidal ZnO QDs based on homoleptic organozinc precursors in the presence of sulfoxide ligands.[46,47] One particularly effective combination involves diethylzinc (Et_2Zn) and the short-chain ligand dimethyl sulfoxide (DMSO). The resulting QDs possess an easily removable solvating layer while remaining redispersible in DMSO and DMSO–water mixtures.[46] This labile organic shell supports charge mobility and enables its application as an electron transport layer in perovskite solar cells.[48,49] Other sulfoxides have also been explored as ligands in stoichiometric reactions and were further investigated for their diversified photocatalytic properties.[47]

While a wide variety of ligand classes have been employed in ZnO QD research, the rational selection of ligand systems remains a key bottleneck in tailoring nanomaterial properties for specific applications. In this context, zwitterionic ligands are of particular interest.[33,50] Although they do not fit neatly into the X/L/Z classification system proposed by M. Green,[51,52] they exhibit strong and often reversible surface interactions due to their spatially separated positive and negative charges. This amphoteric characteristic makes them especially attractive for the design of advanced nanomaterials.[53,54] Although reports remain limited, zwitterionic ligands have been successfully applied to a wide range of systems, including noble metals (Au,[55–57] Ag,[58] Pd,[59] Pt[60]), metal oxides (ZrO_2,[61] TiO_2,[62] Cu_2O,[63] SiO_2[64]), magnetic-type nanoparticles,[65,66] perovskite nanocrystals,[67–71] and semiconductor QDs.[72,73] Zwitterionic compounds have also been used to effectively modify the interface between metal oxide-based electron transport layers and a perovskite layer in solar cells.[74–80] Recently, we explored betaine (*N*,*N*,*N*-trimethylglycine) as a simple model zwitterion-derived ligand in an organometallic synthesis of ZnO QDs.[81] The resulting ZnO QDs demonstrated excellent dispersibility in methanol, enabling the formation of uniform thin films *via* solution processing, which facilitated their integration as electron transport layers in planar perovskite solar cells, achieving power conversion efficiencies around 22% and competitive operational stability.[81] Encouraged by these results, we initiated systematic research to identify a broader range of betaine-like ligands, *i.e.*, electrically neutral compounds featuring spatially separated positive and negative charges. The wet-organometallic approaches presented here are based on a classical OSSOM method, with slight modifications of the oxygen source (air or water), leading to the preparation of a series of QDs stabilized by both long- and short-chain betaines (Scheme 1), whose solubility and colloidal stability have been comprehensively characterized.

2. Experimental

Characterization techniques

HRTEM measurements were performed with a JEOL JEM-2100 operated at an acceleration voltage of 200 kV. Samples were

prepared by slow evaporation of a droplet of a ZnO QD colloidal solution in MeOH (for BET, CAR, SB-8) or in acetone (for DDMAB), respectively, for proligands in two synthetic procedures, deposited on a holey carbon-coated copper grid. The size of ZnO QDs was calculated using image analyses (*i.e.*, a population of at least 100 particles was measured) using ImageJ2x. PXRD data for ZnO QDs were collected with an Empyrean diffractometer (PANalytical) by employing Ni-filtered CuKa radiation from a copper-sealed tube charged with 40 kV voltage and 40 mA current in Bragg–Brentano geometry with a beam divergence of 1 deg in the scattering plane. Diffraction patterns were measured in the range of 20–80 degrees of scattering angle by step scanning with steps of 0.008 degrees. Evaluation of the solvodynamic diameters and zeta potential of the ZnO QDs was performed with a Malvern Zetasizer Nano Z. A solution of QDs was filtered through a 0.2 μm filter before the analysis to remove any dust particles. Mean diameter values (SD), as well as zeta potential (ξ), were measured in three individual experiments. The measurements were performed at room temperature. FTIR spectra were measured with a Bruker Vertex 800V. Measurements were conducted with an ATR attachment. TGA was carried out with a TA Instruments SDT Q600 instrument under a flow of artificial air, to a maximum. 1000 °C, at a heating rate of 5 °C min^{-1} (flow rate of 100 mL min^{-1}). Open alumina crucibles 5 mm in diagonal were used. Optical absorption (UV-Vis) spectra of QD colloidal solutions were collected with a Hitachi U-2910 spectrophotometer. A standard quartz cell (Hellma) with a 10 mm path length was used and rinsed with the appropriate solvent before each run. PL measurements were carried out with a Hitachi Fluorescence Spectrophotometer F-7000. Fluorescence quantum yields (PLQY) and fluorescence lifetime (τ) in the solid-state were recorded on a Quantaurus–QY and a Quantaurus–Tau (Hamamatsu), respectively.

General remarks

All manipulations involving organozinc compounds were carried out under a dry, oxygen-free, inert gas (nitrogen) atmosphere in carefully dried glassware using standard Schlenk techniques. The reagents were purchased from commercial vendors, including diethyl zinc (ABCR), betaine (Fluka), L-carnitine (TCI), DDMAB (Merck), and SB-8 (Fluorochem), and were used as received. HPLC-grade solvents, such as THF (J.T. Baker) and hexane (POCh), were purified with the SPS-800 MBraun solvent purification system prior to contact with organozinc compounds. The purification process and dispersibility tests of the resulting nanomaterials were conducted using various solvents, including methanol (POCh), ethanol (POCh), diethyl ether (POCh), DMSO (POCh), acetone (POCh), THF (POCh), toluene (POCh), DMF (POCh), chloroform (POCh), dichloromethane (POCh), and hexane (POCh), all of which were used as received (p.a. grade). Citrate-phosphate buffer solutions, *i.e.*, pH 4.00 ± 0.05 and pH 7.00 ± 0.05, and borate buffer solution pH 9.00 ± 0.05 (Chempur) were used as received. Deionized water (Merck MilliPore) used in the reactions was degassed by the freeze–pump–thaw method.

General procedure of zwitterion-derived ligand-coated ZnO QD preparation *via* a modified OSSOM approach

ZnO QDs coated by zwitterionic-type ligands were synthesised using a previously reported air-promoted wet-organometallic procedure applied for betaine-coated ZnO QDs.[81] Briefly, Et_2Zn in hexane (0.41 mL of a 2.42 M solution in hexane, 1 mmol) was added dropwise to a stirred solution of selected zwitterion-type compound, *i.e.*, 1.0 mmol of L-carnitine (161 mg), 0.5 mmol or DDMAB (140 mg) or 0.5 mmol of SB-8 (140 mg), respectively, in THF (5 mL) at −78 °C (dry ice–isopropanol bath). The reaction mixture was then allowed to warm to room temperature and stirred for an additional 24 h.

In the second step, the resulting mixture was exposed to air and stirred vigorously for approximately 4–6 days under ambient air conditions at room temperature (22–27 °C). After this time, an iridescent and colloidally stable solution (**ZnO-DDMAB QDs**) or a white suspension (for **ZnO-CAR, ZnO-SB-8**, and **ZnO-NDSB-201 QDs**) exhibiting yellowish fluorescence was obtained. The **ZnO-DDMAB QDs** were subsequently precipitated from the THF solution using hexane (10 mL), washed with EtOH (3 mL), and dried. **ZnO-CAR** and **ZnO-SB-8 QDs** were isolated by sedimentation, washed with MeOH (1 mL, **ZnO-CAR QDs**) or EtOH (1 mL, **ZnO-SB-8 QDs**), and subsequently dried under vacuum. The purified ZnO QDs were then used for further characterization. The nanostructures obtained in this manner will be named according to the **ZnO-ligand name QD** scheme.

ZnO-BET QDs: IR (ATR) $\bar{\upsilon}$ = 3373 (vw), 2962 (w), 1574 (w), 1403 (w), 1333 (vw), 1259 (m), 1206 (w), 1083 (s), 1016 (vs), 865 (w), 792 (vs), 701 (vw), 425 (vs) cm^{-1}.

ZnO-DDMAB QDs: IR (ATR): $\bar{\upsilon}$ = 3360 (w), 3033 (w), 2956 (w), 2923 (s), 2852 (m), 2328 (vw), 2117 (vw), 1997 (vw), 1573 (vs), 1485 (m), 1467 (s), 1390 (vs), 1332 (m), 1305 (m), 1262 (w), 1125 (w), 1065 (m), 1035 (m), 986 (w), 931 (m), 876 (m), 792 (m), 722 (s), 657 (s), 474 (vs) cm^{-1}.

ZnO-CAR QDs: IR (ATR): $\bar{\upsilon}$ = 3360 (vw), 2962 (vw), 2873 (vw), 2161 (vw), 2024 (vw), 1973 (vw), 1577 (w), 1476 (vw), 1397 (w), 1299 (vw), 1205 (vs), 1146 (vs), 978 (vw), 958 (vw), 938 (vw), 911 (vw), 871 (vw), 719 (vw), 635 (w), 624 (m), 552 (m), 501 (vs) cm^{-1}.

ZnO-SB-8 QDs: IR (ATR): $\bar{\upsilon}$ = 3407 (w), 3039 (vw), 2958 (w), 2926 (w), 2856 (w), 1614 (vw), 1489 (vw), 1467 (w), 1420 (w), 1377 (vw), 1342 (vw), 1318 (vw), 1300 (vw), 1260 (w), 1175 (s), 1066 (s), 1033 (vs), 922 (w), 861 (w), 797 (s), 757 (w), 728 (m), 661 (w), 605 (m), 448 (vs) cm^{-1}.

ZnO-NDSB-201 QDs: IR (ATR) $\bar{\upsilon}$ = 3380 (w), 3026 (vw), 2962 (w), 1761 (vw), 1576 (w), 1486 (w), 1410 (w), 1323 (vw), 1298 (vw), 1260 (m), 1192 (s), 1163 (m), 1138 (m), 1089 (s), 1058 (s), 1029 (vs), 864 (w), 797 (vs), 689 (s), 608 (s), 584 (m), 520 (s), 481 (vs), 447 (vs) cm^{-1}.

Preparation of zwitterion-derived ligand-coated ZnO QDs *via* a controlled water addition method

Similarly to the previous procedure, Et_2Zn in hexane (0.41 mL of a 2.42 M solution in hexane, 1 mmol) was added dropwise to a stirred solution of the selected zwitterion-type compound in THF (5 mL) at −78 °C. Then, degassed water (54 μL, 3 mmol)

was added dropwise, and the reaction mixture was allowed to warm to room temperature under continuous stirring. Yellowish fluorescence appeared immediately for **ZnO-BET^{h} QDs** and **ZnO-CAR^{h} QDs**, whereas it developed after a few hours for **ZnO-SB-8^{h} QDs** and **ZnO-DDMAB^{h} QDs**. The resulting ZnO QDs formed non-transparent white suspensions, with a higher tendency toward sedimentation observed for **ZnO-BET^{h} QDs** and **ZnO-CAR^{h} QDs**, and the lowest for **ZnO-DDMAB^{h} QDs**. Subsequently, the ZnO QDs were precipitated from the THF solution using hexane (8 mL) and rewashed with MeOH (3 mL). Additionally, **ZnO-CAR^{h} QDs** were further precipitated with acetone (10 mL) from the methanolic solution. Finally, the ZnO QDs were dried under vacuum and used for further characterization. The nanostructures obtained in this manner will be named according to the **ZnO-ligand name^{h} QD** scheme, where the superscript ***h*** distinguishes the hydrolytic method.

ZnO-BET^{h} QDs: IR (ATR) $\bar{\upsilon}$ = 3379 (vw), 3048 (vw), 3020 (vw), 2966 (vw), 1624 (s), 1479 (vw), 1457 (vw), 1417 (w), 1385 (w), 1339 (w), 1260 (w), 1242 (vw), 1089 (m), 1019 (m), 984 (w), 954 (w), 935 (w), 892 (m), 798 (m), 712 (w), 427 (vs) cm^{-1}.

ZnO-DDMAB^{h} QDs: IR (ATR) $\bar{\upsilon}$ = 3407 (w), 3025 (vw), 2959 (w), 2919 (m), 2852 (m), 2160 (vw), 2018 (vw), 1968 (vw), 1673 (vw), 1587 (vs), 1467 (w), 1382 (s), 1336 (vw), 1306 (w), 1260 (m), 1220 (vw), 1189 (vw), 1088 (m), 1061 (m), 1018 (s), 928 (w), 874 (w), 799 (s), 721 (w), 659 (w), 447 (vs) cm^{-1}.

ZnO-CAR^{h} QDs: IR (ATR) $\bar{\upsilon}$ = 3305 (w), 2965 (vw), 2360 (vw), 2334 (vw), 2121 (vw), 1572 (m), 1477 (w), 1390 (m), 1260 (w), 1210 (vw), 1179 (vw), 1089 (m), 1019 (m), 961 (w), 938 (w), 898 (w), 865 (w), 798 (m), 687 (m), 431 (vs) cm^{-1}.

ZnO-SB-8^{h} QDs: IR (ATR) $\bar{\upsilon}$ = 3423 (w), 3039 (vw), 2958 (vw), 2926 (w), 2856 (vw), 1646 (vw), 1486 (w), 1467 (w), 1419 (vw), 1377 (vw), 1305 (vw), 1262 (w), 1180 (m), 1095 (m), 1035 (s), 956 (w), 912 (w), 868 (w), 801 (m), 727 (m), 659 (w), 604 (m), 433 (vs) cm^{-1}.

ZnO-NDSB-201^{h} QDs: IR (ATR) $\bar{\upsilon}$ = 3513 (vw), 3387 (vw), 3129 (vw), 3095 (vw), 3065 (vw), 3026 (vw), 2955 (vw), 2351 (vw), 2110 (vw), 1990 (vw), 1629 (vw), 1502 (vw), 1486 (w), 1469 (vw), 1335 (vw), 1323 (vw), 1299 (vw), 1260 (vw), 1239 (vw), 1218 (vw), 1192 (m), 1163 (m), 1139 (m), 1031 (s), 971 (w), 901 (vw), 851 (vw), 831 (vw), 788 (w), 772 (m), 751 (w), 691 (m), 610 (m), 584 (w), 520 (s), 481 (vs), 433 (vs), 418 (vs), 405 (vs) cm^{-1}.

General procedure of carboxylic-ligand-coated ZnO QD preparation using the OSSOM approach

Briefly, Et_2Zn in hexane (0.41 mL of a 2.42 M solution in hexane, 1 mmol) was added dropwise to a stirred solution of selected carboxylic acid, *i.e.*, 1 mmol of 2-(2-methoxyethoxy)acetic acid (MAA-H, 135 mg) or decanoic acid (C10-H, 172 mg) or heptadecanoic acid (C17-H, 270 mg), respectively, in THF (5 mL) at −78 °C (dry ice–isopropanol bath). Then, the reaction mixture was allowed to warm to room temperature and stirred for an additional 24 h. In the second step, the resulting mixture was exposed to air and stirred vigorously up to *ca.* 4–6 days under ambient air conditions at room temperature (*ca.* 22–27 °C). Note that the resulting ZnO QDs were characterized using TEM, UV-Vis, PL and DLS, and all samples were found to be consistent with the respective systems previously reported, exhibiting similar size, morphology, crystal structure, and optical properties. **ZnO-MAA QDs:** λ_{abs} = 332 nm, λ_{em} = 520 nm, d = 5.18 ± 0.98 nm (estimated from TEM data), SD (*Z*-average) = 10.97 nm (in THF); **ZnO-C10 QDs:** λ_{abs} = 331 nm, λ_{em} = 518 nm, d = 4.92 ± 0.60 nm (estimated from TEM data), SD (Z-average) = 6.84 nm (in THF); **ZnO-C17 QDs:** λ_{abs} = 335 nm, λ_{em} = 525 nm, and d = 4.52 ± 0.58 nm (estimated from TEM data), SD (Z-average) = 12.60 nm (in THF).

3. Results and discussion

Building upon our previous achievement,[81] in which ZnO QDs stabilised with betaine were successfully implemented as electron transport layers in perovskite solar cells, we aimed to further expand the versatility of this strategy by exploring structurally diverse zwitterionic ligands (Scheme 1) within the organometallic synthetic framework. Given that simple betaine enables the formation of colloidal ZnO QDs in low-volatility alcohols while preserving favorable photoluminescence and morphology, we hypothesized that other zwitterion-derived ligands could provide comparable or even enhanced stabilization. Accordingly, we decided to investigate a broader range of zwitterionic organic ligands (*i.e.*, electrically neutral compounds featuring spatially separated positive and negative charges) as proligands for the synthesis of ZnO QDs. In addition to betaine (BET), which was discussed previously,[81] we selected four other commercially available zwitterions with systematically varied structures: L-carnitine (CAR), *N*-dodecyl-*N*,*N*-(dimethylammonio)butyrate (DDMAB), sulfobetaine-8 (SB-8), and 3-(1-pyridino)-1-propane sulfonate (NDSB-201) (see Scheme 1). The selected zwitterionic-type ligands not only differ in their alkyl chain length but also feature diverse head groups, including carboxylate-based ligands (BET, CAR, DDMAB) and sulfonate-based ligands (SB-8, NDSB-201), thereby providing a broad spectrum of electronic and steric environments for ZnO QD stabilisation. Thus, structural modifications of their head groups, connecting bridges, and tail substituents allowed us to evaluate their performance as stabilizers for ZnO QDs and dispersants in various solvent systems. Importantly, all ligands share a comparable alkyl backbone length (*i.e.*, –CH_2–CH_2–CH_2– moiety) between their charged groups (except BET, which contains a single –CH_2– unit), while CAR additionally features a hydroxyl group centrally positioned along the chain. Furthermore, DDMAB and SB-8 are distinguished by the presence of long hydrophobic alkyl tails attached to the nitrogen atom, unlike CAR and BET, which possess only methyl substituents, while NDSB-201 contains a positively charged pyridinium ring (Scheme 1).

3.1. Preparation and characterization of zwitterionic-type ligand-coated ZnO QDs

A series of ZnO QDs coated with selected zwitterion-derived ligands were prepared using modified OSSOM approaches as a model platform for synthesis.[14,16–27,30] In the first step, an

equimolar mixture of commercially available diethylzinc (Et_2Zn) and the respective zwitterion was prepared in tetrahydrofuran (THF). Subsequently, two alternative reaction pathways were applied to initiate ZnO formation: (*i*) exposure of the as-prepared mixture to ambient air (Scheme 1, path *i*) or (*ii*) controlled addition of water at a stoichiometric ratio of 3 : 1 with respect to the zinc precursor (Scheme 1, path *ii*). Both pathways afford ZnO QDs coated with the corresponding ligand shell, herein abbreviated as **ZnO-X** for materials obtained *via* air exposure (path *i*), and as **ZnO-X^h** for those synthesised *via* the controlled water addition method (path *ii*) (where X = BET, CAR, DDMAB, SB-8, NDSB-201), respectively. The **ZnO-BET**, **ZnO-CAR**, and **ZnO-SB-8**, **ZnO-NDSB-201 QD** dispersions formed white suspensions; whereas **ZnO-DDMAB QDs** exhibited a stable, opalescent dispersion in post-synthetic THF solutions. In contrast, materials obtained *via* the controlled water addition method (path *ii*) showed a higher tendency toward sedimentation in the parent solution. The resulting ZnO QDs were thoroughly characterized through a suite of analytical techniques, including high-resolution transmission electron microscopy (HRTEM), powder X-ray diffraction (PXRD), dynamic light-scattering (DLS) measurements, thermogravimetric analysis (TGA), Fourier transform infrared spectroscopy (FTIR), UV/Vis spectrophotometry, and photoluminescence (PL) spectroscopy, alongside assessments of their absolute quantum yield (PLQY), luminescence lifetimes (τ), colloidal stability, and dispersibility across a range of organic solvents, water, and buffered media.

The HRTEM micrographs revealed that the ZnO QDs appeared either as isolated particles or as small aggregates, allowing the determination of size distributions and the calculation of average diameters for representative populations (Fig. 1). The average diameters of ZnO QDs, determined from HRTEM images, were 6.7 $\pm$ 0.6 nm (**ZnO-BET**), 5.2 $\pm$ 0.7 nm (**ZnO-DDMAB**), 6.0 $\pm$ 1.3 nm (**ZnO-CAR**), 5.5 $\pm$ 0.8 nm (**ZnO-SB-8**), and 7.6 $\pm$ 1.3 nm (**ZnO-NDSB-8**) for the air-exposure method. In contrast, the direct hydrolysis method yielded slightly smaller particles for most systems: 4.8 $\pm$ 0.9 nm (**ZnO-BET^h**), 4.9 $\pm$ 0.7 nm (**ZnO-DDMAB^h**), 5.6 $\pm$ 0.6 nm (**ZnO-CAR^h**), 5.5 $\pm$ 1.1 nm (**ZnO-SB-8^h**), with a larger diameter of 8.4 $\pm$ 1.6 nm observed for **ZnO-NDSB-8^h** QDs (Fig. S1 in the SI). Furthermore, HRTEM analysis confirmed the crystalline structure of the ZnO QDs, which was identified as the wurtzite phase based on PXRD patterns (Fig. 4b and Fig. S2 in the SI). The characteristic broadening of diffraction peaks, typical for nanoscale materials, enabled the estimation of mean nanocrystal sizes using the Scherrer equation, providing complementary data to the HRTEM-based measurements (see Fig. 4b and Fig. S2 in the SI). For most samples, the sizes obtained *via* both methods were consistent within their respective standard deviations (Fig. S3 in the SI). Overall, the air-exposure method resulted in a noticeable increase in QD sizes, suggesting that under slower hydrolysis/oxidation conditions (path *i*), the structural characteristics of the zwitterionic ligands

exert a pronounced influence on the resulting inorganic core dimensions. In contrast, under accelerated reaction conditions (path *ii*), the particle sizes appear largely independent of ligand chain identity. Notably, the ZnO QDs synthesised using NDSB-201 represent an exception, consistently exhibiting slightly larger average diameters relative to other systems. To provide a more comprehensive and dynamic characterisation beyond simple core size estimation, solvodynamic diameters (SD) reported as *Z*-average values (see Table 1) were measured for organic solvent dispersions using dynamic light scattering (DLS). As expected, these values were larger than those of the inorganic core alone due to the presence of the organic ligand shell stabilising the core and solvent molecules in the outer sphere[82,83] (for details, see Fig. S4, S5, and Table S2 in the SI). Notably, QDs synthesised *via* the direct hydrolysis strategy (path *ii*) exhibited significantly higher SD values compared to those obtained *via* air exposure (path *i*). The observed increase in solvodynamic diameter for ZnO QDs under accelerated hydrolysis conditions (path *ii*) can be attributed to the organisation and dynamics of the surface ligands. Rapid nucleation and growth limit the time available for ligands to form a dense and well-ordered coating, resulting in a more loosely packed organic shell. This less compact ligand layer, combined with associated solvent molecules, leads to an effective expansion of the solvodynamic diameter, even though the inorganic core remains comparatively small. Conversely, under slower hydrolysis conditions, ligands have sufficient time to arrange more uniformly on the QD surface, allowing for better passivation of the core and yielding nanocrystals whose solvodynamic size more accurately reflects the core dimensions. Nevertheless, with the exception of **ZnO-SB-8^h** dispersion, all measured solvodynamic diameters remained below 100 nm, satisfying the general size criterion for classification as nanomaterials (Table 1). In general, the SD distributions of zwitterion-derived ligand-coated ZnO QDs exhibit a predominantly monodisperse characteristic, as confirmed by size distribution profiles based on intensity, volume, and number (Fig. S4 and S5), as well as polydispersity index (PDI) values ranging from 0.129 to 0.284. All relevant parameters, including those significant for colloidal stability – such as ζ-potential values derived from DLS measurements – are summarized in Table 1 or in Table S2 in the SI. It is well established that stable colloidal dispersions typically exhibit surface charges with absolute ζ-potential values $|\zeta| \geq$ 20–30 mV.[84] Remarkably, all ZnO QDs obtained in this study, regardless of the zwitterionic ligand used, exhibit positive surface charges in methanol dispersions, clearly indicating their inherent colloidal stability (see Table 1).

Complementary Fourier-transformed infrared spectroscopy (FTIR) and thermogravimetric (TGA) were employed to gain insight into the nature and composition of the organic–inorganic interface in ZnO QDs. All FTIR spectra exhibit a characteristic, intense band attributed to the Zn–O stretching vibration ν(Zn–O) in the range 501–448 cm^{-1} (Fig. 2, for details see the experimental details provided in the SI). Additionally, a broad absorption band in the 3500–3200 cm^{-1} region corresponds to O–H stretching vibrations, which is also observed in the pure zwitterionic proligands (BET, CAR, DDMAB). For zwitterion-type ligands bearing long alkyl chains (DDMAB and

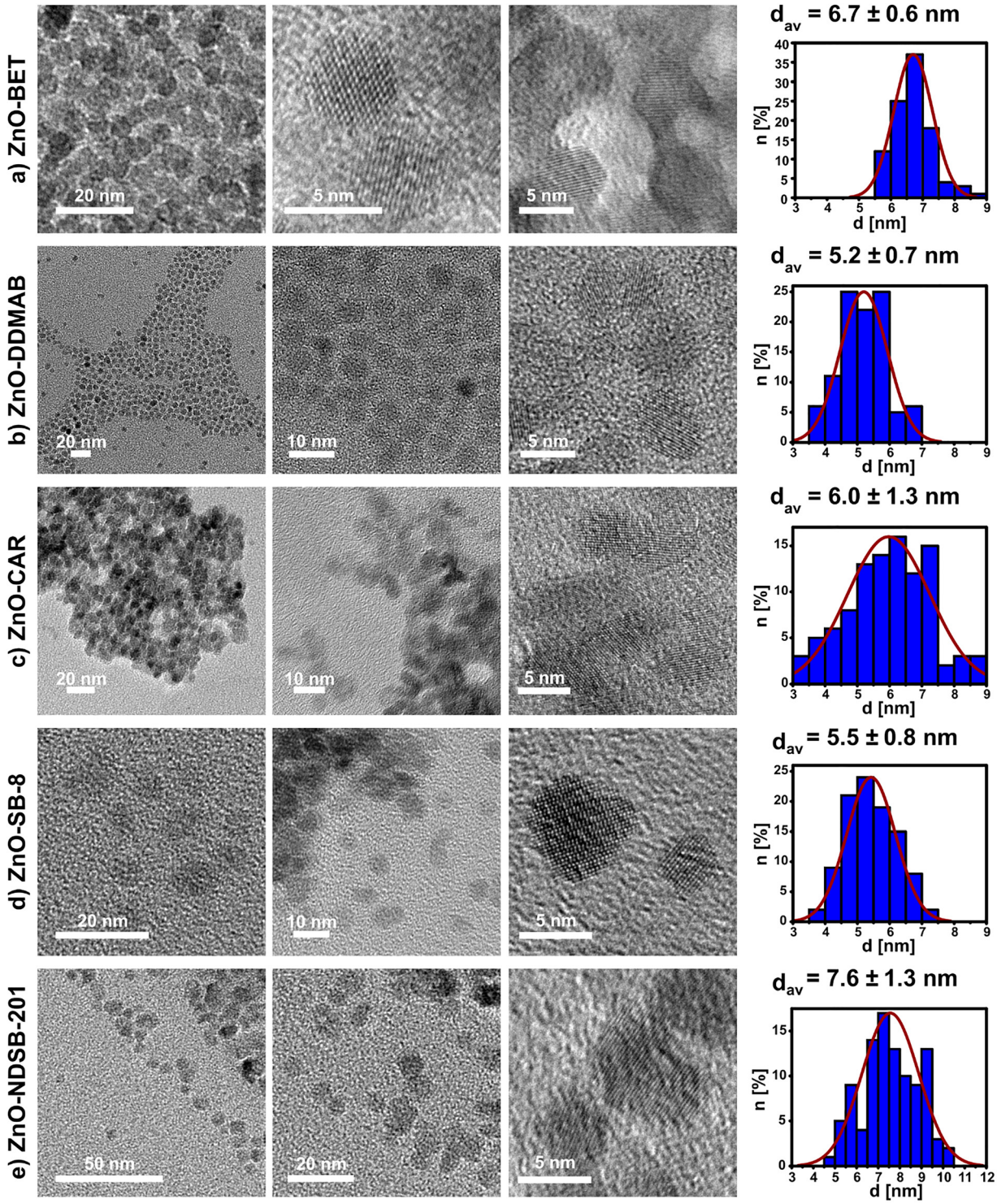

Fig. 1 Representative HRTEM micrographs of **ZnO-X QDs** along with their size distributions and Gaussian approximation prepared by the air-exposure method.

SB-8), the presence of four distinct bands confirms their structure: the asymmetric CH_3– stretching around 2959 cm^{-1}, asymmetric and symmetric –CH_2– stretching at 2922 and 2853 cm^{-1}, respectively, and the C–C rocking mode of the alkyl chain at ~722 cm^{-1}. In contrast, BET, CAR, and NDSB-201 show only the $\nu_{as}(CH_3)$ band at 2962 cm^{-1}, 2956 cm^{-1}, and 2966 cm^{-1}, respectively. In the FTIR spectra of ZnO QDs coated with carnitine moieties, a distinct overlapping band assigned to the C–O stretching vibration of secondary alcohols is observed. Notably, a significant shift exceeding 100 cm^{-1} is detected between the two synthetic methods, 1202 cm^{-1} and 1147 cm^{-1} for **Zn-CAR** (path *i*) and 1091 cm^{-1} and 1022 cm^{-1}

Table 1 Average solvodynamic size, surface charge, and optical features of ZnO quantum dots

		SD [nm] (PDI)	ξ [mV]	$\lambda_{abs}/\lambda_{em}$ [nm]	FWHM [nm]	PLQY [%]	τ [ns]	E_g [eV]
ZnO-BET	*i*	14.5 (0.251)^{MeOH}	27.9 ± 1.0	342/540^{MeOH}	132	11.7^{ex335}	2304.0	3.43
	ii	86.9 (0.183)^{EtOH}	7.8 ± 5.9	335/535^{EtOH}	134	4.6^{ex335}	718.3	3.35
ZnO-DDMAB	*i*	9.9 (0.129)^{PhMe}	16.9 ± 6.8	308/492^{THF}	122	20.8^{ex330}	1169.4	3.77
	ii	14.8 (0.173)^{THF}	27.7 ± (—)	334/533^{THF}	140	41.8^{ex330}	867.3	3.45
ZnO-CAR	*i*	12.2 (0.179)^{MeOH}	17.9 ± 10.6	330/521^{MeOH}	128	18.2^{ex330}	1464.6	3.53
	ii	59.6 (0.284)^{MeOH}	27.2 ± 10.5	351/555^{MeOH}	134	3.8^{ex330}	656.2	3.25
ZnO-SB-8	*i*	35.96 (0.269)^{MeOH}	20.6 ± 8.6	341/552^{MeOH}	138	11.8^{ex335}	1508.3	3.40
	ii	299.8 (0.205)^{MeOH}	36.0 ± 5.7	346/544^{MeOH}	134	27.5^{ex335}	1363.2	3.26
ZnO-NDSB-201	*i*	95.5 (0.132)^{MeOH}	29.2 ± 9.3	345/547^{MeOH}	139	10.4^{ex335}	1336.4	3.30
	ii	n.d.	n.d.	353/549^{MeOH}	139	1.1^{ex330}	680.7	3.29

Abbreviations: n.d. – no data provided; ZnO QDs prepared *via* air-exposure (path *i*) and controlled water addition (path *ii*); ^{ex} – excitation wavelength (nm).

for the water-assisted method (path *ii*) – suggesting coordination of the zwitterion-derived ligand with the ZnO surface (note that these signals are very weak in pure carnitine). From a coordination chemistry perspective, the carboxylate group vibrations are particularly relevant for BET, CAR, and DDMAB ligands. For example, **ZnO-CAR QDs** exhibit two typical COO^- bands at 1577 cm^{-1} (asymmetric) and 1397 cm^{-1} (symmetric), whereas the C=O band at 1685 cm^{-1}, present in the pure CAR proligand spectrum, disappears upon coordination to the surface of QDs. In contrast, **ZnO-BET^h** retain a C=O absorption band at 1621 cm^{-1}, whereas ZnO-BET QDs exhibit two relatively broad bands with a maximum at 1573 cm^{-1} and 1403 cm^{-1}, each resulting from the overlap of multiple components, indicating the presence of diverse coordination modes of the betaine-derived ligands on the surface, both as X- or L-type. **ZnO-DDMAB^h QDs** exhibit analogous strong COO^- bands at 1573 and 1390 cm^{-1}. The sulfonate group in SB-8 is evidenced by strong symmetric and asymmetric SO_3^- stretching bands at 1175 cm^{-1} and around 1033–1066 cm^{-1}. Of particular interest is the emergence of a dominant band at 1480 cm^{-1} in the spectrum of pure SB-8 within the 1730–1340 cm^{-1} region. In **ZnO-SB-8 QDs**, an additional strong band appears at 1614 cm^{-1} (path *i*) and 1646 cm^{-1} (path *ii*), which may indicate specific interactions with the ZnO surface. Although all zwitterions used share a quaternary ammonium moiety ($C-N^+$) responsible for their positive charge, these groups do not exhibit characteristic IR absorption bands.[85]

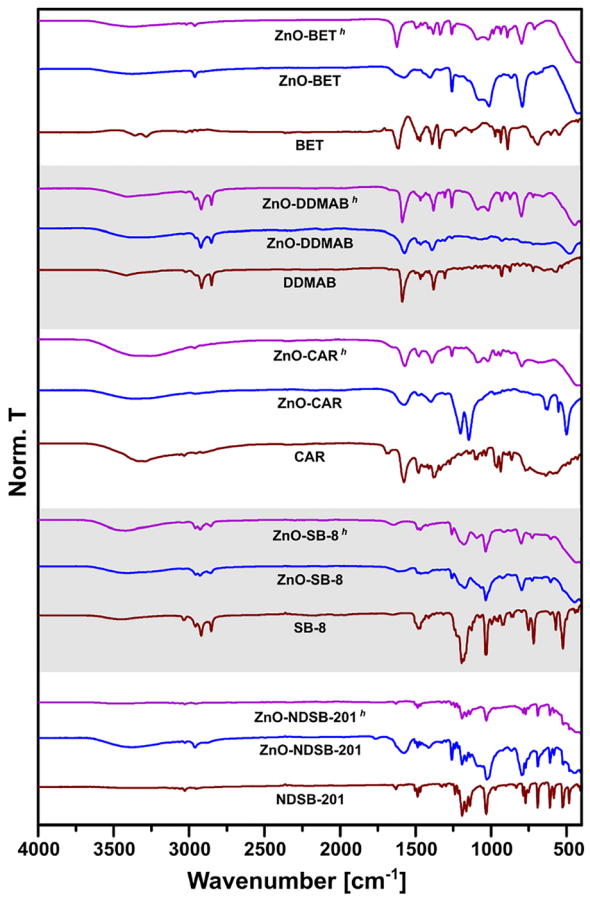

Fig. 2 FTIR spectra of betaines and sulfobetaines' proligands (red line), ZnO QDs prepared by method *i* (blue line) or method *ii* (magenta line).

Thermogravimetric analysis (TGA) of purified ZnO QDs (for details of the purification procedure see the Experimental Section), reveals gradual mass loss profiles associated with the decomposition of the organic components, which is likely attributable to the presence of multiple ligand-type species (including applied solvents) and various forms of ligand. In contrast, a sharp one- or two-step decomposition pathway is observed for the pure zwitterions (the latter in the case of SB-8, see Fig. S6 in the SI). The total weight loss for the two synthetic protocols ranges from 35% to 77%, although the decomposition profiles differ notably. A particularly marked difference is observed for betaine-coated ZnO QDs, where the final decomposition temperature of the organic phase is 600 °C for method (path *i*) and 350 °C for method (path *ii*), implying the presence of several components (including various types of betaine-derived ligands and decomposition of solvents used during the purification process) in the air-exposure route. For comparison, in the TG profile of pure betaine, one main decomposition step is present, with a maximum decomposition rate at 302 °C.

All ZnO QDs exhibit a characteristic broad absorption in the ultraviolet region, with maximum absorbance near 330 nm, and a relatively narrow, symmetric emission band centred around 530 nm (for details see Table 1, Fig. 3a, and Fig. S7). The visible yellow luminescence of the ZnO QDs upon UV

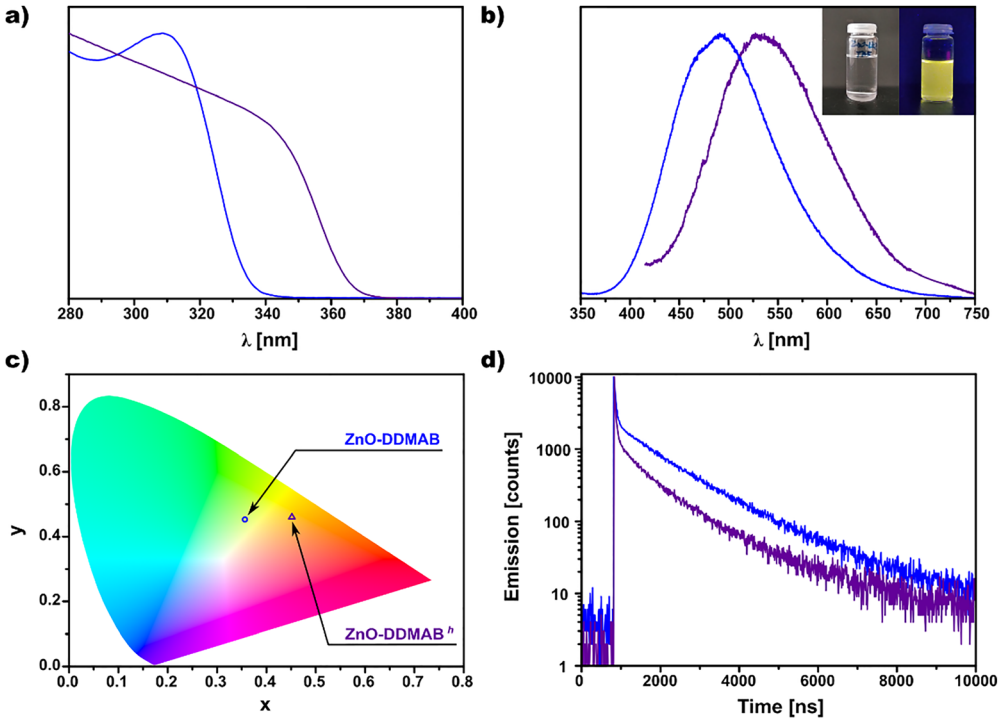

Fig. 3 (a) Absorbance spectra (λ_{abs}: **ZnO-DDMAB** = 308 nm, **ZnO-DDMAB^{h}** = 334 nm), (b) emission spectra (λ_{abs}: **ZnO-DDMAB** = 492 nm, **ZnO-DDMAB^{h}** = 533 nm) with photographs of the colloidal dispersions, (c) chromaticity coordinates in the CIE diagram showing the emission colour (with [*x*, *y*] coordinates of **ZnO-DDMAB QDs**: [0.3425, 0.4128] and **ZnO-DDMAB^{h} QDs**: [0.446, 0.4549]), and (d) luminescence decay of ZnO QDs stabilised by DDMAB. Sample types: (a) and (b) THF dispersions; (c) and (d) solid samples.

excitation is further supported by their chromaticity coordinates plotted on the CIE diagram (Fig. 3b and Fig. S8). Photoluminescence quantum yield (PLQY) measurements, on solid-state samples, reveal a substantial difference between the two synthetic pathways, clearly favouring the air-exposure method (path *i*). The ratios of quantum yields between two synthetic approaches ($PLQY_i/PLQY_{ii}$) for ZnO QDs stabilised with BET, CAR, and NDSB-201 are 2.5, 4.8, and 9.5, respectively, whereas ZnO QDs stabilised with DDMAB and SB-8 exhibit lower ratios of 0.5 and 0.4. Interestingly, for ZnO QDs capped with long-chain zwitterion-derived ligands, exceptionally high PLQY values were recorded in individual syntheses using the direct hydrolysis method (path *ii*): **ZnO-DDMAB^{h} QDs** reached 41.8% ($\tau < 1$ μs), and **ZnO-SB-8^{h} QDs** reached 27.5% ($\tau > 1$ μs). In contrast, **ZnO-BET^{h}** and **ZnO-CAR^{h}** exhibited rather moderate PLQYs (6.2% and 4.6%, respectively). For ZnO QDs, a PLQY above 20% is already considered an excellent result, highlighting the high quality of the nanostructures obtained in this study.

Photoluminescence lifetime (τ) was also assessed as an important optical parameter[86] (see Table 1). For all samples synthesised *via* the air-exposure method (path *i*), τ exceeded 1 μs and was comparable to other systems derived from organometallic approaches,[14–30] whereas for QDs obtained *via* the water addition method (path *ii*), values were consistently shorter, *i.e.*, in the nanosecond range (see Table 1). The τ_i/τ_{ii} ratios – 3.2 (for **BET**), 1.3 (for **CAR**), 2.2 (for **DDMAB**), 1.1 (for **SB-8**), and 2.0 (for **NDSB-201**) – underscore the significant effect of synthesis conditions on exciton recombination dynamics (see the details provided in Tables S3–S7 in the SI). The difference between the two preparation pathways can be attributed to a combination of factors, including partial destabilisation of ligand–QD interactions and changes in the local electronic environment at the QD surface, both of which could be induced by solvent/water adsorption and promote non-radiative recombination. It is worth noting that long photoluminescence lifetimes, corresponding to slower electron–hole recombination, are advantageous for sensing or photocatalytic applications, as the excited electron remains available for longer. Shorter lifetimes, indicating faster recombination, are more desirable for optoelectronic devices such as LEDs, meaning that our ZnO QDs can potentially cover a wide spectrum of applications depending on the chosen synthesis and ligand system.

3.2. Solubility and stability of zwitterion-stabilised ZnO quantum dots

Stabilising ligands play a pivotal role in the synthesis of nanomaterials, as they govern not only the nucleation and growth dynamics but also critically determine the dispersibility and long-term colloidal stability of the resulting nanostructures in specific solvent environments. Their molecular features – such as polarity, charge distribution, and additional functionality (*i.e.*, the presence of additional reactive sites for post-synthetic modifications or specific functional groups) – directly affect solubility in polar and/or non-polar media, making

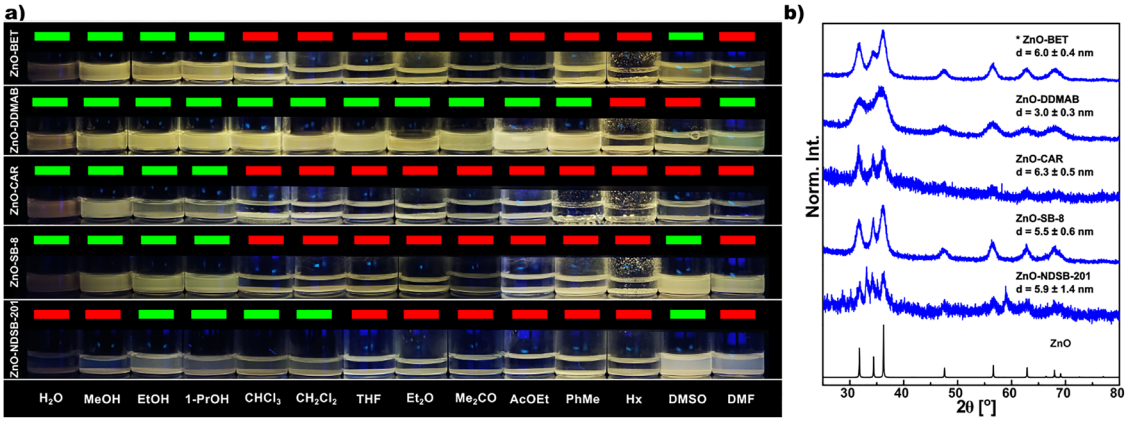

Fig. 4 (a) Photographs of dispersions of **ZnO-X QDs** in selected solvents, with labels indicating stability (green – stable; red – sedimenting). (b) Powder X-ray diffraction patterns of **ZnO-X QDs**, with average sizes estimated using the Scherrer equation.

rational ligand selection essential for tailoring nanomaterial properties to targeted applications. Thus, both the dispersibility and colloidal stability of ZnO QDs were systematically assessed to evaluate the practical utility of the zwitterion-derived ligand-stabilised ZnO QDs. To explore the behaviour of these systems under more diluted conditions, solubility tests were conducted using a standardised protocol in which 0.1 mL of the THF-based parent post-reaction solution was added to 1 mL of selected solvents (see Fig. 4a). Notably, all ZnO QDs exhibited stable colloidal behaviour in methanol (ζ-potential values provided in Table 1), with similarly stable dispersions observed in ethanol and 1-propanol. The ZnO coated with **DDMAB** QDs demonstrated superior solubility and stability across a broad spectrum of common laboratory solvents, including methanol, ethanol, 1-propanol, DMSO, DMF, acetone, and even diethyl ether, remaining dispersed for extended periods (up to 18 days), with hexane being the only exception due to its known precipitation effect (Fig. 4a). Other systems showed limited stability in methanol and chloroform, where the luminescence quenching effect became apparent (for details, see the photos in Fig. S8–S10 in the SI). Stability over time was further supported by spectroscopic measurements (UV-Vis and PL). Absorbance and emission spectra of selected samples, including **ZnO-DDMAB QDs**, were recorded at regular intervals. The results revealed that although a slight bathochromic shift and band broadening occurred over several weeks, spectral parameters eventually stabilised, indicating long-term preservation of optical properties (Fig. S12 in the SI). Moreover, **ZnO-DDMAB QDs** exhibited outstanding solubility (up to 500 mg mL^{-1}), followed by **ZnO-CAR** (20–40 mg mL^{-1}, with minor flocculation). In contrast, **ZnO-BET** and **ZnO-SB-8** displayed significantly lower solubility (<0.8 mg mL^{-1} and 0.8–1.2 mg mL^{-1}, respectively), correlating with visible sedimentation and limited optical clarity (Fig. S11). For comparison, ZnO QDs prepared *via* the OSSOM approach with classical carboxylate ligands (*e.g.*, methoxyethoxyacetate, undecanoate, and heptadecanoate ligands) were also evaluated. These ZnO nanocrystals demonstrated poor solubility in polar media and suffered from luminescence quenching in solvents such as water, acetone, and alcohols (Fig. S15–S17). While they remained stable in aprotic solvents (THF, diethyl ether, toluene, DMSO, and DMF), their overall solvent compatibility was more limited compared to their zwitterion-derived ligand-coated analogues (for details see the SI). These findings underscore the unique advantage of zwitterionic-type ligands in achieving broad solvent compatibility, sustained colloidal stability, and preservation of luminescence properties across diverse environments.

3.3. Aqueous stability and pH-dependent behaviour of ZnO QDs

Given the promising colloidal behaviour of zwitterion-derived ligand-coated ZnO QDs in organic solvents, we next turned our attention to evaluating their performance in aqueous environments under various pH conditions. Prepared water dispersions of all ZnO QDs revealed a slight tendency toward sedimentation, accompanied by significant photoluminescence quenching in the case of **ZnO-BET**, **ZnO-CAR**, **ZnO-SB-8**, and **ZnO-NDSB-201**, as well as time-dependent PL quenching in the case of **ZnO-DDMAB QDs**. Encouraged by the relatively good solubility in polar organic solvents (*e.g.*, alcohols, DMSO, DMF) and relatively long-term stability in water, we selected **ZnO-BET QDs** as a model system for extended stability testing. This assessment was conducted in pure water and in three buffered aqueous solutions, *i.e.*, phosphate-citrate buffers at acidic (pH 4) and neutral (pH 7) conditions, and an alkaline borate buffer (pH 9), monitored over 22 days under both visible and UV light, and *via* spectroscopic analysis performed during the first five days. Notably, **ZnO-BET^{h} QDs** exhibited the greatest stability in pure water: photoluminescence was visible throughout the entire volume without stirring up to day 4, and the sediment retained emissive properties for over 22 days. In contrast, the acidic buffer induced the most rapid destabilisation, yet even in this environment, the sediment preserved weak yellow emission for up to five days. Interestingly, while emission from QDs in the alkaline buffer also diminished by day 5, the sediment remained luminescent for over five months in this environment. Next, in the neutral buffer (pH 7), spectral shifts were

observed beginning on day 5: a hypsochromic shift in the emission maximum and a bathochromic shift in absorption were recorded in the transparent supernatant, persisting for over five months (Fig. S19). This behaviour suggests the formation of hybrid nanostructures comprising ZnO QDs and ionic buffer components such as sodium phosphate, citric acid, and potassium chloride, as well as dynamic compositional reorganisation within the surface-stabilising layer. These interactions likely altered the electron transfer processes, as indicated by the unusually small Stokes shift ($\Delta\lambda$ = 53 nm; λ_{abs} = 406 nm, λ_{em} = 459 nm) and a notably wide optical band gap ($\sim$4.0 eV). Photoluminescence quantum yield (PLQY) under these conditions reached 9.2% (λ_{ex} = 400–415 nm), and the narrow emission profile (FWHM = 67 nm) was comparable to that of organic dyes (*e.g.*, fluorescein) and small commercial Cd-based QDs. Simultaneously, DLS measurements indicated a gradual reduction in solvodynamic diameter, while ζ-potential increased from -33.4 mV (day 3) to -10.3 mV (day 10) and -4.4 mV (day 19), indicating dynamic surface reorganisation.

4. Conclusions

Zinc oxide quantum dots are promising semiconductor nanomaterials whose functional properties are strongly influenced by the synthetic methodology. Building on previous work employing simple betaine as a stabilising ligand in air-mediated OSSOM synthesis,[81] this study expands the scope by introducing three additional zwitterionic-type ligands with related structural motifs. We further developed a wet-organometallic approach using diethylzinc and zwitterionic compounds to fabricate high-quality ZnO QDs under mild conditions. Comparative analysis of the resulting materials was carried out on two principal levels: (1) the structural nature of the zwitterionic ligands (short- *vs.* long-chain; betaine *vs.* sulfobetaine) and (2) the mode of precursor transformation (air exposure *vs.* direct water addition). The results demonstrate that the synthetic route exerts a significant influence on the photoluminescence properties of all nanocrystals and on particle size in the case of short-chain ligands such as BET and CAR. The obtained ZnO QDs exhibit stable colloidal dispersions and tunable optical properties (with photoluminescence lifetimes $\langle\tau\rangle$ $\sim$1 μs and PLQYs ranging from 3.8% to 41.8%), positioning them as attractive candidates for applications in optoelectronic devices—including solar cells, where reproducible thin-film deposition from selected solvents is crucial—as well as in biological systems, exemplified by the aqueous-stable **ZnO-BET QDs**. In summary, the integration of zwitterionic organic ligands within a wet-organometallic framework provides and tunable strategy for generating luminescent, colloidally stable ZnO QDs with small core sizes and broad medium compatibility. By demonstrating precise control over particle size, surface passivation, and photoluminescence efficiency (up to 41.8% PLQY), this work establishes these hybrid inorganic–organic nanostructures as highly promising candidates for next-generation optoelectronic and biomedical applications, offering new avenues for energy harvesting, sensing, and biologically relevant technologies.

Author contributions

The manuscript was written with contributions from all authors. All authors have given approval to the final version of the manuscript.

Conflicts of interest

There are no conflicts to declare.

Data availability

The data supporting this article have been included as part of the supplementary information (SI). Supplementary information: detailed synthetic procedures, characterisation data, and additional figures and tables that illustrate and complement the results presented in the article. See DOI: https://doi.org/10.1039/d5tc03681j.

Acknowledgements

The authors acknowledge the financial support from the National Science Centre, Grant MAESTRO 11, No. 2019/34/A/ST5/00416 (J. L.). Research was cofounded by POB Technologie Materiałowe (M. W.-P.) and YOUNG (Z. D.) of Warsaw University of Technology within the Excellence Initiative: Research University (IDUB) programme.

References

1 H. Morkoç and Ü. Özgür, *Zinc Oxide: Fundamentals, Materials and Device Technology*, Wiley-VCH, Weinheim, 2009.
2 H. M. Xiong, *Adv. Mater.*, 2013, **25**, 5329–5335.
3 J. Luo, Y. Wang and Q. Zhang, *Solar Energy*, 2018, **163**, 289–306.
4 S. Raha and M. Ahmaruzzaman, *Nanoscale Adv.*, 2022, **4**, 1868–1925.
5 B. Clarke and K. Ghandi, *Small*, 2023, **19**, 2302864.
6 J. Van Embden, S. Gross, K. R. Kittilstved and E. Della Gaspera, *Chem. Rev.*, 2023, **123**, 271–326.
7 J. M. Nam, J. S. Owen and D. V. Talapin, *Acc. Chem. Res.*, 2023, **56**, 2265–2266.
8 L. Spanhel and M. A. Anderson, *J. Am. Chem. Soc.*, 1991, **113**, 2826–2833.
9 E. A. Meulenkamp, *J. Phys. Chem. B*, 1998, **102**, 5566–5572.
10 L. Spanhel, *J. Sol–Gel Sci. Technol.*, 2006, **39**, 7–24.
11 A. E. Danks, S. R. Hall and Z. Schnepp, *Mater. Horizons*, 2016, **3**, 91–112.
12 D. W. Bahnemann, C. Kormann and M. R. Hoffmann, *J. Phys. Chem.*, 1987, **91**, 3789–3798.

13 S. Arya, P. Mahajan, S. Mahajan, A. Khosla, R. Datt, V. Gupta, S.-J. Young and S. K. Oruganti, *ECS J. Solid State Sci. Technol.*, 2021, **10**, 023002.
14 D. Lee, M. Wolska-Pietkiewicz, S. Badoni, A. Grala, J. Lewiński and G. De Paëpe, *Angew. Chem., Int. Ed.*, 2019, **58**, 17163–17168.
15 N. Olejnik-Fehér, M. Jędrzejewska, M. Wolska-Pietkiewicz, D. Lee, G. De Paëpe and J. Lewiński, *Small*, 2024, **20**, 2309984.
16 J. Paczesny, M. Wolska-Pietkiewicz, I. Binkiewicz, Z. Wróbel, M. Wadowska, K. Matuła, I. Dzięcielewski, D. Pociecha, J. Smalc-Koziorowska, J. Lewiński and R. Hołyst, *Chem. – Eur. J.*, 2015, **21**, 16941–16947.
17 J. Paczesny, M. Wolska-Pietkiewicz, I. Binkiewicz, M. Wadowska, Z. Wróbel, K. Matuła, W. Nogala, J. Lewiński and R. Hołyst, *ACS Appl. Mater. Interfaces*, 2016, **8**, 13532–13541.
18 A. Grala, M. Wolska-Pietkiewicz, W. Danowski, Z. Wróbel, J. Grzonka and J. Lewiński, *Chem. Commun.*, 2016, **52**, 7340–7343.
19 M. Wolska-Pietkiewicz, K. Tokarska, A. Grala, A. Wojewódzka, E. Chwojnowska, J. Grzonka, P. J. P. J. Cywiński, K. Kruczała, Z. Sojka, M. Chudy, M. Chudy and J. Lewiński, *Chem. – Eur. J.*, 2018, **24**, 4033–4042.
20 A. Grala, M. Wolska-Pietkiewicz, Z. Wróbel, T. Ratajczyk, J. Kuncewicz and J. Lewiński, *Mater. Chem. Front.*, 2018, **2**, 1004–1111.
21 M. Wolska-Pietkiewicz, K. Tokarska, A. Wojewódzka, K. Wójcik, E. Chwojnowska, J. Grzonka, P. J. Cywiński, M. Chudy and J. Lewiński, *Sci. Rep.*, 2019, **9**, 1–14.
22 E. Chwojnowska, M. Wolska-Pietkiewicz, J. Grzonka and J. Lewiński, *Nanoscale*, 2017, **9**, 14782–14786.
23 M. Terlecki, S. Badoni, M. K. Leszczyński, S. Gierlotka, I. Justyniak, H. Okuno, M. Wolska-Pietkiewicz, D. Lee, G. De Paëpe and J. Lewiński, *Adv. Funct. Mater.*, 2021, **31**, 2105318.
24 S. Badoni, M. Terlecki, S. Carret, J. F. Poisson, T. Charpentier, H. Okuno, M. Wolska-Pietkiewicz, D. Lee, J. Lewiński and G. De Paëpe, *J. Am. Chem. Soc.*, 2024, **146**, 27655–27667.
25 A. Borkenhagen, K. Sokołowski, P. W. Majewski, I. Justyniak, P. Roś, A. M. Cieślak and J. Lewiński, *Nat. Commun.*, 2025, **16**, 10254.
26 M. Wolska-Pietkiewicz, A. Grala, I. Justyniak, D. Hryciuk, M. Jędrzejewska, J. Grzonka, K. J. Kurzydłowski and J. Lewiński, *Chem. – Eur. J.*, 2017, **23**, 11856–11865.
27 A. Borkenhagen, M. Wolska-Pietkiewicz, I. Binkiewicz, Ł. Richter, R. Zbonikowski, J. Paczesny and J. Lewiński, *ACS Appl. Mater. Interfaces*, 2025, **17**, 36212–36225.
28 M. Wolska-Pietkiewicz, A. Świerkosz, I. Justyniak, A. Grala, K. Sokołowski and J. Lewiński, *Dalton Trans.*, 2016, **45**, 18813–18816.
29 M. Terlecki, I. Justyniak, M. K. Leszczyński, P. Bernatowicz and J. Lewiński, *Dalton Trans.*, 2023, **52**, 2712–2721.
30 A. Wojewódzka, M. Wolska-Pietkiewicz, R. H. Szczepanowski, M. Jędrzejewska, K. Zelga and J. Lewiński, *Nanoscale Adv.*, 2025, **7**, 2677–2685.
31 Z. Wu, S. Yang and W. Wu, *Nanoscale*, 2016, **8**, 1237–1259.
32 M. A. Boles, D. Ling, T. Hyeon and D. V. Talapin, *Nat. Mater.*, 2016, **15**, 141–153.
33 A. Heuer-Jungemann, N. Feliu, I. Bakaimi, M. Hamaly, A. Alkilany, I. Chakraborty, A. Masood, M. F. Casula, A. Kostopoulou, E. Oh, K. Susumu, M. H. Stewart, I. L. Medintz, E. Stratakis, W. J. Parak and A. G. Kanaras, *Chem. Rev.*, 2019, **119**, 4819–4880.
34 J. J. Calvin, A. S. Brewer and A. P. Alivisatos, *Nat. Synth.*, 2022, **1**, 127–137.
35 M. Shim and P. Guyot-Sionnest, *J. Am. Chem. Soc.*, 2001, **123**, 11651–11654.
36 M. Monge, M. L. Kahn, A. Maisonnat and B. Chaudret, *Angew. Chem., Int. Ed.*, 2003, **42**, 5321–5324.
37 M. L. Kahn, M. Monge, V. Collière, F. Senocq, A. Maisonnat and B. Chaudret, *Adv. Funct. Mater.*, 2005, **15**, 458–468.
38 M. L. Kahn, T. Cardinal, B. Bousquet, M. Monge, V. Jubera and B. Chaudret, *ChemPhysChem*, 2006, **7**, 2392–2397.
39 Y. Coppel, G. Spataro, C. Pagès, B. Chaudret, A. Maisonnat and M. L. Kahn, *Chem. – Eur. J.*, 2012, **18**, 5384–5393.
40 Y. Wang, Y. Coppel, C. Lepetit, J. D. Marty, C. Mingotaud and M. L. Kahn, *Nanoscale Adv.*, 2021, **3**, 6088–6099.
41 Z. Zhao, Y. Wang, C. Delmas, C. Mingotaud, J. D. Marty and M. L. Kahn, *Nanoscale Adv.*, 2021, **3**, 6696–6703.
42 K. L. Orchard, M. S. P. Shaffer and C. K. Williams, *Chem. Mater.*, 2012, **24**, 2443–2448.
43 S. Noimark, J. Weiner, N. Noor, E. Allan, C. K. Williams, M. S. P. Shaffer and I. P. Parkin, *Adv. Funct. Mater.*, 2015, **25**, 1367–1373.
44 A. H. M. Leung, A. García-Trenco, A. Phanopoulos, A. Regoutz, M. E. Schuster, S. D. Pike, M. S. P. Shaffer and C. K. Williams, *J. Mater. Chem. A*, 2020, **8**, 11282–11291.
45 C. B. Murray, D. J. Norris and M. G. Bawendi, *J. Am. Chem. Soc.*, 1993, **115**, 8706–8715.
46 M. Wolska-Pietkiewicz, M. Jędrzejewska, K. Tokarska, J. Wielgórska, M. Chudy, J. Grzonka and J. Lewiński, *Chem. Eng. J.*, 2023, **455**, 140497.
47 M. Jędrzejewska, M. Wolska-Pietkiewicz, Z. Drużyński and J. Lewiński, *J. Mater. Chem. C*, 2023, **11**, 15016–15029.
48 D. Prochowicz, M. M. Tavakoli, M. Wolska-Pietkiewicz, M. Jędrzejewska, S. Trivedi, M. Kumar, S. M. Zakeeruddin, J. Lewiński, M. Graetzel and P. Yadav, *Sol. Energy*, 2020, **197**, 50–57.
49 R. D. Chavan, M. Wolska-Pietkiewicz, D. Prochowicz, M. Jędrzejewska, M. M. Tavakoli, P. Yadav, C. K. Hong and J. Lewiński, *Adv. Funct. Mater.*, 2022, **32**, 2205909.
50 J. B. Schlenoff, *Langmuir*, 2014, **30**, 9625–9636.
51 M. L. H. Green, *J. Organomet. Chem.*, 1995, **500**, 127–148.
52 J. Owen, *Science*, 2015, **347**, 615–616.
53 Betaines, https://goldbook.iupac.org/terms/view/B00637, (accessed 6 April 2022).
54 M. J. Rosen and J. T. Kunjappu, *Surfactants and Interfacial Phenomena*, John Wiley & Sons, Ltd, 2012, pp. 502–530.
55 W. Zhou, L. Ling, Y. Du, W. He, Q. Xia, C. Yao and X. Li, *Langmuir*, 2019, **35**, 13031–13039.

56 Y. Takagai, R. Miura, A. Endo and W. L. Hinze, *Chem. Commun.*, 2016, **52**, 10000–10003.
57 P. Pallavicini, G. Chirico, M. Collini, G. Dacarro, A. Donà, L. D'Alfonso, A. Falqui, Y. Diaz-Fernandez, S. Freddi, B. Garofalo, A. Genovese, L. Sironi and A. Taglietti, *Chem. Commun.*, 2011, **47**, 1315–1317.
58 M. Pisárčik, M. Lukáč, J. Jampílek, F. Bilka, A. Bilková, Ľ. Pašková, F. Devínsky, R. Horáková and T. Opravil, *J. Mol. Liq.*, 2018, **272**, 60–72.
59 X. Wen, S. Lerch, Z. Wang, B. Aboudiab, A. R. Tehrani-Bagha, E. Olsson and K. Moth-Poulsen, *Langmuir*, 2020, **36**, 1745–1753.
60 L. M. Martínez-Prieto, I. Cano, A. Márquez, E. A. Baquero, S. Tricard, L. Cusinato, I. Del Rosal, R. Poteau, Y. Coppel, K. Philippot, B. Chaudret, J. Cámpora and P. W. N. M. Van Leeuwen, *Chem. Sci.*, 2017, **8**, 2931–2941.
61 G. K. Sidhu and R. Kumar, *Appl. Surf. Sci.*, 2017, **392**, 598–607.
62 D. L. Liao and B. Q. Liao, *J. Photochem. Photobiol. A Chem.*, 2007, **187**, 363–369.
63 M. J. Woźniak-Budych, Ł. Przysiecka, B. M. Maciejewska, D. Wieczorek, K. Staszak, M. Jarek, T. Jesionowski and S. Jurga, *ACS Biomater. Sci. Eng.*, 2017, **3**, 3183–3194.
64 W. A. El-Said, A. S. Moharram, E. M. Hussein and A. M. El-Khawaga, *Mater. Chem. Phys.*, 2018, **211**, 123–136.
65 G. Leem, S. Sarangi, S. Zhang, I. Rusakova, A. Brazdeikis, D. Litvinov and T. R. Lee, *Cryst. Growth Des.*, 2009, **9**, 32–34.
66 S. Mondini, M. Leonzino, C. Drago, A. M. Ferretti, S. Usseglio, D. Maggioni, P. Tornese, B. Chini and A. Ponti, *Langmuir*, 2015, **31**, 7381–7390.
67 F. Krieg, S. T. Ochsenbein, S. Yakunin, S. Ten Brinck, P. Aellen, A. Süess, B. Clerc, D. Guggisberg, O. Nazarenko, Y. Shynkarenko, S. Kumar, C. J. Shih, I. Infante and M. V. Kovalenko, *ACS Energy Lett.*, 2018, **3**, 641–646.
68 Q. A. Akkerman, G. Rainò, M. V. Kovalenko and L. Manna, *Nat. Mater.*, 2018, **17**, 394–405.
69 R. Grisorio, F. Fasulo, A. B. Muñoz-García, M. Pavone, D. Conelli, E. Fanizza, M. Striccoli, I. Allegretta, R. Terzano, N. Margiotta, P. Vivo and G. P. Suranna, *Nano Lett.*, 2022, **22**, 4437–4444.
70 S. H. Noh, K. H. Lee, H. S. Yang, J. Jung, E. H. Suh, J. G. Oh, U. Paik, S. C. Park and J. Jang, *Chem. Eng. J.*, 2024, **481**, 148127.
71 C. Cueto, M. Hu, T. P. Russell and T. Emrick, *J. Am. Chem. Soc.*, 2024, **146**, 8189–8197.
72 P. S. Nair, K. P. Fritz and G. D. Scholes, *Small*, 2007, **3**, 481–487.
73 E. Muro, T. Pons, N. Lequeux, A. Fragola, N. Sanson, Z. Lenkei and B. Dubertret, *J. Am. Chem. Soc.*, 2010, **132**, 4556–4557.
74 K. Choi, J. Lee, H. Il Kim, C. W. Park, G. W. Kim, H. Choi, S. Park, S. A. Park and T. Park, *Energy Environ. Sci.*, 2018, **11**, 3238–3247.
75 Q. Chen, X. Yang, Y. Zhou and B. Song, *New J. Chem.*, 2021, **45**, 15118–15130.
76 Z. Qin, Y. Chen, X. Wang, N. Wei, X. Liu, H. Chen, Y. Miao and Y. Zhao, *Adv. Mater.*, 2022, **34**, 2203143.
77 H. Zou, Y. Duan, S. Yang, D. Xu, L. Yang, J. Cui, H. Zhou, M. Wu, J. Wang, X. Lei, N. Zhang and Z. Liu, *Small*, 2023, **19**, 2206205.
78 X. Wang, J. Jiang, Z. Liu, A. Li, T. Miyasaka and X. F. Wang, *Small*, 2024, **20**, 2400356.
79 H. Kim, K. Choi, G. W. Yoon, D. Kim, D. H. Lee, Y. Choi, H. S. Jung, S. Song and T. Park, *Adv. Energy Mater.*, 2024, **14**, 2401263.
80 F. Ansari, L. Zheng, L. Pfeifer, F. T. Eickemeyer, S. M. Zakeeruddin, N. Lempesis, V. Carnevali, A. Vezzosi, V. Sláma, T. Georges, U. Gunes, L. Emsley, M. K. Nazeeruddin, U. Rothlisberger, P. J. Dyson and M. Grätzel, *Adv. Mater.*, 2025, **37**, 2501075.
81 R. Runjhun, E. A. Alharbi, Z. Drużyński, A. Krishna, M. Wolska-Pietkiewicz, V. Škorjanc, T. P. Baumeler, G. Kakavelakis, F. Eickemeyer, M. Mensi, S. M. Zakeeruddin, M. Graetzel and J. Lewiński, *Energy Environ. Mater.*, 2024, **7**, e12720.
82 E. H. M. Sakho, E. Allahyari, O. S. Oluwafemi, S. Thomas and N. Kalarikkal, Dynamic Light Scattering (DLS), ed. S. Thomas, R. Thomas, A. K. Zachariah and R. K. Mishra, in *Thermal and Rheological Measurement Techniques for Nanomaterials Characterization*, Elsevier, 2017, pp. 37–49, DOI: 10.1016/B978-0-323-46139-9.00002-5.
83 K. Takahashi, H. Kato, T. Saito, S. Matsuyama and S. Kinugasa, *Anal. Part. Part. Syst. Charact.*, 2008, **25**, 31–38.
84 S. Mourdikoudis, R. M. Pallares and N. T. K. Thanh, *Nanoscale*, 2018, **10**, 12871–12934.
85 G. Socrates, *Infrared and Raman characteristic group frequencies, Tables and charts*, John Wiley & Sons, Ltd, 3rd edn, 2004.
86 W. Thor, J.-C. G. Bünzli, K.-L. Wong and P. A. Tanner, *Adv. Photonics Res.*, 2025, **6**, 2400081.

